

Ion-Neutral Drift Velocity as a Diagnostic of Dust Growth and Magnetic Field in Star-Forming Environments

HARUKA FUKIHARA,¹ YUSUKE TSUKAMOTO,¹ HIROYUKI HIRASHITA,² DORIS ARZOUMANIAN,³ AND YOSHIAKI MISUGI^{4,5}

¹*Kagoshima University*

²*Osaka University*

³*Kyusyu University*

⁴*National Astronomical Observatory of Japan*

⁵*Kyusyu Sangyo University*

ABSTRACT

Recent observations have revealed that the ion–neutral drift velocity in star-forming molecular clouds and dense cores is on the order of $\sim 100 \text{ m s}^{-1}$. Theoretical studies have shown that, in ambipolar diffusion—the process responsible for the differential motion between ions and neutrals—the dust size distribution has a significant impact on the magnetic resistivities. In this study, we perform simulations to investigate how dust growth through accretion and coagulation affects the ion–neutral drift velocity in molecular clouds and cores. We find that, on core scales, both dust growth and a magnetic field strength of $200 \mu\text{G}$ are required to reproduce the observed drift velocity. We suggest that measurements of ion–neutral drift velocity, particularly on core scales, may serve as a new diagnostic to constrain the dust size distribution and magnetic field strength in such environments.

Keywords: Molecular clouds (1072) — Magnetic fields (994) — Dust physics (2229)

1. INTRODUCTION

Magnetic fields in star-forming clouds are primarily probed by Zeeman splitting and by dust polarization. Zeeman observations in H_I, OH, and CN provide direct line-of-sight field strengths in diffuse and dense gas (C. Heiles & T. H. Troland 2005; T. H. Troland & R. M. Crutcher 2008; E. Falgarone et al. 2008; R. M. Crutcher 2012). However, detections of Zeeman splitting require bright, suitable transitions, and high signal-to-noise. Therefore, the measurements are inevitably sparse and subject to selection effects.

Dust polarization observations constrain the magnetic-field orientation in the plane of the sky. Furthermore, magnetic field strengths can be inferred using the Davis–Chandrasekhar–Fermi (DCF) method, which relates the dispersion of polarization angles to the gas velocity dispersion (S. Chandrasekhar & E. Fermi 1953). Large surveys such as the JCMT POL-2 BISTRO project now provide cloud-to-core coverage of polarization maps (S. Coudé et al. 2019; Y. Doi et al. 2020; K. Pattle et al. 2019, 2021; D. Arzoumanian et al. 2021; J. Hwang et al. 2021; A. R. Lyo et al. 2021; T.-C.

Ching et al. 2022; D. Ward-Thompson et al. 2023; J.-W. Wang et al. 2024)

However, DCF-based estimates may carry substantial systematics (projection, beam and line-of-sight averaging, density and turbulence assumptions, order-unity calibration factors), and recent assessments highlight non-negligible biases and uncertainties (R. M. Crutcher 2012; R. Skalidis & K. Tassis 2021; C.-Y. Chen et al. 2022). Given these complementary but limited techniques: Zeeman splitting is precise but observationally restrictive, whereas DCF method is widely applicable but uncertain, there is clear motivation to develop additional, independent diagnostics of magnetic field strength in star-forming regions.

Ambipolar diffusion, the slippage of magnetic fields through partially ionized gas mediated by ion–neutral drift, has long been recognized as a key ingredient in star formation theory (e.g., L. Mestel & L. Spitzer 1956; F. H. Shu et al. 1987). By considering ambipolar diffusion, the induction equation can be written as

$$\frac{\partial \mathbf{B}}{\partial t} = \nabla \times (\mathbf{v} \times \mathbf{B}) + \nabla \times \left[\eta_A ((\nabla \times \mathbf{B}) \times \hat{\mathbf{B}}) \times \hat{\mathbf{B}} \right], \quad (1)$$

where η_A is the ambipolar resistivity and $\hat{\mathbf{B}}$ the unit vector along \mathbf{B} . The value of η_A is calculated from the ionization balance, which is controlled by cosmic-ray

ionization, gas-phase recombination, and the adsorption of charged particles onto dust grains.

The crucial role of dust grains in regulating the ionization degree and ambipolar resistivities was clarified by early work that explicitly treated dust-controlled ionization and coupling in molecular clouds and cores (e.g., B. G. Elmegreen 1979; T. Umebayashi & T. Nakano 1980; T. Nakano & T. Umebayashi 1986; T. Umebayashi & T. Nakano 1990; R. Nishi et al. 1991); see also T. Nakano et al. (2002). Subsequently, axisymmetric thin-disk/1.5D calculations incorporating dust-dependent magnetic resistivities were applied to the dynamical evolution of molecular cloud cores (G. E. Ciolek & T. C. Mouschovias 1993, 1994, 1995). Multi-dimensional non-ideal MHD studies further linked this microscopic physics to core collapse and disk formation, exploring the impact of Ohmic dissipation, Hall effect, and ambipolar diffusion with varying the ionization chemistry (e.g., Z.-Y. Li et al. 2011; Y. Tsukamoto et al. 2015; K. Tomida et al. 2015; J. Masson et al. 2016; J. Wurster et al. 2016; B. Zhao et al. 2016; W. Xu & M. W. Kunz 2021; A. Tritsis et al. 2022; Y. Kobayashi et al. 2023; Y. Tsukamoto et al. 2023; Y. Tsukamoto 2024; A. Tritsis et al. 2025). It is commonly understood that the ionization degree, and hence η_A , is sensitive to the abundance of small grains (B. Zhao et al. 2021; Y. Tsukamoto & S. Okuzumi 2022).

On the observational side, several efforts have been made to constrain ion-neutral drift directly by comparing matched-resolution ion and neutral tracers. H.-W. Yen et al. (2018) found that the ion-neutral velocity difference on $\sim 10^2$ – 10^3 AU scales in B335 is small (\lesssim a few $\times 10^2$ m s $^{-1}$), implying strong coupling between the magnetic field and gas on these scales. On cloud scales, J. E. Pineda et al. (2021) reported systematic ion-neutral linewidth differences in Barnard 5 filament (N₂H⁺ broader than NH₃), and additional detections are emerging in a prestellar core (Arzoumanian & Speziano et al., in prep.). Nevertheless, interpreting ion-neutral drift measurements requires careful consideration: line-of-sight averaging, projection, tracer chemistry/optical depth, and large-scale field geometry can bias inferred drifts (e.g., M. Houde et al. 2009; H.-b. Li & M. Houde 2008; A. Tritsis et al. 2025).

Despite the well-established importance of dust grains for ambipolar diffusion, and hence ion-neutral drift, the explicit connection between dust size evolution and ion-neutral drift on cloud-to-core scales has received comparatively little attention. Given the strong sensitivity of η_A to the small-grain population and the growing observational evidence of ion-neutral drift, it is timely to reassess how the evolution of the dust size distributions

affects the ion-neutral drift velocity and how ion-neutral drift measurements can constrain magnetic fields and dust properties.

In this context, from molecular clouds to dense cores, there are several observations that suggest an evolving dust size distribution. The “coreshine” phenomenon: mid-IR scattered light from dense cores may require micron-sized grains (L. Pagani et al. 2010; J. Steinacker et al. 2010, 2015). Submillimeter observations also show changes of the spectral index of dust opacity in envelope scale (W. Kwon et al. 2009, 2015; L. Cacciapuoti et al. 2024). These results suggest possible grain growth from cloud to core, implying that gas-phase chemical reactions and hence the gas coupling to the magnetic field can change across these environments.

In this study, we investigate how magnetic field strength and key microphysical processes, especially dust size evolution, affect the ion–neutral drift velocity induced by ambipolar diffusion, denoted as v_{drift} , and how its observed values can constrain these quantities. We consider two representative environments, a molecular cloud and a dense core, and evaluate v_{drift} on each scale.

This paper is organized as follows. In Section 2, we describe our cloud and core models, the dust evolution model, and the formulation used to evaluate the ambipolar resistivity and the resulting ion–neutral drift velocity v_{drift} . In Section 3, we present the time evolution of the dust size distribution and the resulting v_{drift} , and we compare our results with observations. In Section 4, we discuss the implied constraints on the physical parameters from the perspective of reproducing the observed drift velocity, and we summarize our main conclusions and future prospects.

2. METHOD

2.1. Dust evolution

In this study, we calculated the dust size evolution considering the accretion and coagulation.

The time evolution of the dust size distribution is given by the formulation of H. Hirashita & S. Aoyama (2019),

$$\frac{\partial \rho_d(m, t)}{\partial t} = \left[\frac{\partial \rho_d(m, t)}{\partial t} \right]_{\text{acc}} + \left[\frac{\partial \rho_d(m, t)}{\partial t} \right]_{\text{coag}}, \quad (2)$$

where $\rho_d(m, t)$ is the mass density of the dust grains which have a mass of m at a time of t .

For accretion, we follow the formulation presented in (H. Hirashita 2012).

$$\frac{\partial n_d(a, t)}{\partial t} + \frac{\partial}{\partial a} [n_d(a, t) \dot{a}] = 0. \quad (3)$$

$$\dot{a} = \xi(t)a/\tau(a) \quad (4)$$

$$\xi(t) \equiv n_X(t)/n_{X,\text{tot}} \quad (5)$$

$\tau(a)$ in Equation (4) is accretion time scale and is assumed as

$$\tau(a) \equiv \frac{a}{\frac{n_{X,\text{tot}} m_X S}{f_X \rho_{\text{mat}}} \left(\frac{k_B T_{\text{gas}}}{2\pi m_X} \right)^{1/2}}. \quad (6)$$

where m_X is the mass of element X . In this study, we consider the accretion of O, which subsequently becomes H₂O on the grain surface. f_X is the mass fraction of the element in the dust grain material, and we adopted $f_X = 16/18 = 0.89$. S is the sticking probability and we adopted $S = 0.3$. k_B and T_{gas} are Boltzmann constant and gas temperature, respectively, for which we assume $T_{\text{gas}} = 10$ K. ρ_{mat} is the material density and we consider this as a parameter (see Section 2.3). $n_{X,\text{tot}}$ is the number density of element X and is described as

$$n_{X,\text{tot}} = Z_m x(X) n_{\text{gas}}, \quad (7)$$

where Z_m is metallicity and we assume $Z_m = 1$ Z_⊙. $x(X)$ is the solar abundance of X , and we assume $x(O) = 4.35 \times 10^{-4}$ based on the commonly adopted interstellar value of $x(O) \sim 10^{-4}$ (e.g., C. Ceccarelli et al. 2018). With these values, dust-to-gas mass ratio becomes 1.4 after accretion. n_{gas} is the number density of gas.

$\xi(t)$ is the fraction of the element in gas phase. We adopted $\xi = 0.9$ at initial state and its subsequent decrease is treated as depletion according to

$$\frac{d\xi}{dt} = -\frac{3f_X\xi(t)}{m_X n_{X,\text{tot}}} \int_0^\infty \frac{\sigma(m, t)}{\tau(m)} dm. \quad (8)$$

The time evolution of grain size distribution by coagulation between grains with the masses of m_1 and m_2 (with the radius of a_1 and a_2) is expressed as

$$\begin{aligned} \left[\frac{\partial \rho_d(m, t)}{\partial t} \right]_{\text{coag}} &= -m \rho_d(m, t) \int_0^\infty \alpha(m_1, m) \rho_d(m_1, t) dm_1 \\ &+ \int_0^\infty \int_0^\infty \alpha(m_1, m_2) \rho_d(m_1, t) \rho_d(m_2, t) \\ &\times m_1 \delta(m - m_1 - m_2) dm_1 dm_2. \end{aligned} \quad (9)$$

Here, α represents the collision efficiency and is given by

$$\alpha(m_1, m_2) \equiv \frac{\sigma_{1,2} \Delta V}{m_1 m_2}, \quad (10)$$

where $\sigma_{1,2} = \pi(a_1 + a_2)^2$ and ΔV are respectively collisional cross-section and relative velocity between two grains.

For the relative velocity between grains, we consider contributions from Brownian motion and turbulence-induced motion, following the model of C. W. Ormel & J. N. Cuzzi (2007).

$$\Delta V = \sqrt{(\Delta V_{\text{BM}})^2 + (\Delta V_{\text{turb}})^2} \quad (11)$$

Figure 1 shows the relative velocity model of two grains with the same radius in a gas of number density $n_{\text{gas}} = 10^6 \text{ cm}^{-3}$ employed in this study. We neglect the bouncing and fragmentation due to the grain-grain collision.

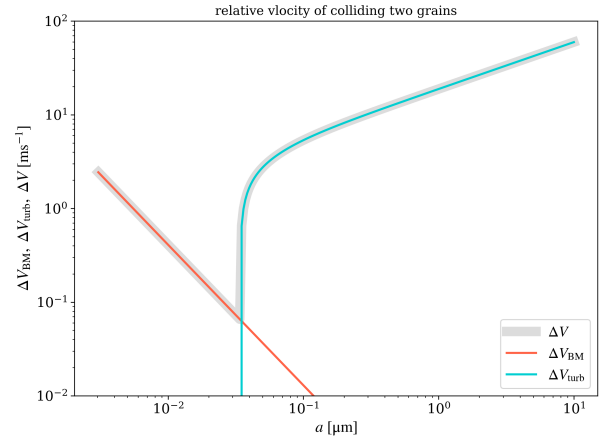


Figure 1. Relative velocity model of two colliding grains introduced in this study. The plot shows the case where the two grains have the same radius ($a_1 = a_2 = a$) and collide in a gas at $n_{\text{gas}} = 10^6 \text{ cm}^{-3}$ with a Mach number of $\mathcal{M} = 2$. ΔV_{BM} represents the contribution from the Brownian motion, whereas ΔV_{turb} represents the contribution from turbulent motion. $\Delta V = \sqrt{(\Delta V_{\text{BM}})^2 + (\Delta V_{\text{turb}})^2}$.

2.2. Ionization chemistry and ion-neutral drift velocity calculation

For the ionization chemistry and resistivity, we follow the analytical framework of Y. Tsukamoto & S. Okuzumi (2022) with one modification appropriate for our cold, low-density conditions.

The ionization equilibrium equation in gas including dust grains adsorption is given as,

$$\zeta n_{\text{gas}} - s_i u_i n_i \overline{(\sigma_d \langle \tilde{J}_i(I, Z) \rangle)} n_d - \beta n_i n_e = 0, \quad (12)$$

$$\zeta n_{\text{gas}} - s_e u_e n_e \overline{(\sigma_d \langle \tilde{J}_e(I, Z) \rangle)} n_d - \beta n_i n_e = 0, \quad (13)$$

where n_{gas} , n_i , n_e and n_d are the number densities of the neutral gas, ion, electron and dust grains, respectively. I and Z are indices for dust size and dust charging and $\langle f \rangle$ and \tilde{f} denote the average over Z and I , respectively. The first term represents the ionization of neutral particles in the gas phase, the second term represents the

adsorption of charged particles onto dust grain surfaces, and the third term represents the recombination of gas-phase ions. ζ is the ionization rate. s_i and s_e are the sticking probability of ion and electron to dust grain surface. u_i and u_e are the average velocity of ion and electron. $\tilde{J}_{i(e)}$ is the effective cross-section normalized by $\sigma_d(I) = \pi(a_d(I))^2$, where a_d is the dust radius. β is the recombination rate of ions.

In the low- τ limit ($\tau(I) \equiv a_I k_B T / e^2 \ll 1$) appropriate for our cold, low-density conditions, the dust charge distribution concentrates to $Z \in \{-1, 0, +1\}$. Therefore, we only consider these three charge states. The detailed balance between adjacent dust charge states yields

$$\epsilon n_d(I, Z) \tilde{J}_i(I, Z) = n_d(I, Z + 1) \tilde{J}_e(I, Z + 1), \quad (14)$$

with $\epsilon \equiv (n_i s_i u_i) / (n_e s_e u_e)$.

Then, charge neutrality condition is written as an equation of ϵ as,

$$n_i(\epsilon) - n_e(\epsilon) + n_d \overline{Z}(\epsilon) = 0, \quad (15)$$

and we solve for ϵ in this equation using the Newton-Raphson method to obtain n_i , n_e , n_d .

Using obtained n_i , n_e , n_d , the ohmic(σ_O), Hall(σ_H), Pedersen(σ_P) conductivities are calculated as follows.

$$\sigma_O = \sum_s \frac{c}{B} n_s \beta_s, \quad (16)$$

$$\sigma_H = - \sum_s \frac{c}{B} \frac{n_s q_s \beta_s^2}{1 + \beta_s^2}, \quad (17)$$

$$\sigma_P = \sum_s \frac{c}{B} \frac{n_s q_s \beta_s}{1 + \beta_s^2}. \quad (18)$$

The subscript s denotes the particle species (ions, electrons, and dust). q_s is the charge of each particle species and c is the speed of light. The dimensionless Hall parameter β_s is defined as the ratio of the cyclotron frequency of charged particles to their collision frequency with neutral gas particles. This parameter is expressed as

$$\beta_s = \frac{q_s B}{m_s c} \frac{m_s + m_{\text{gas}}}{\langle \sigma v \rangle_s m_{\text{gas}} n_{\text{gas}}}, \quad (19)$$

where $\langle \sigma v \rangle_s$ is the collisional momentum transfer rate between charged particles and neutrals and is derived from equations in C. Pinto & D. Galli (2008). m_s and m_{gas} are the mass of each particle species and the mean mass of the gas, respectively.

From the above electrical conductivities, the ambipolar resistivity η_A is calculated as,

$$\eta_A = \frac{c^2}{4\pi} \left(\frac{\sigma_P}{\sigma_H^2 + \sigma_P^2} - \frac{1}{\sigma_O} \right). \quad (20)$$

Then, we can estimate the ion-neutral drift velocity as,

$$v_{\text{drift}} = \eta_A \frac{(\nabla \times \mathbf{B}) \times \mathbf{B}}{|\mathbf{B}|^2} \sim \frac{\eta_A}{L}, \quad (21)$$

where L is a characteristic length scale and assumed to be the Jeans length $L = \lambda_J$. Note that, under the assumption that the magnetic field is frozen in the gas, it is physically natural to expect that magnetic field gradients and curvatures will arise at the Jeans length scale, which is the typical scale for the motion of self-gravitating gas. This assumption that ion-neutral drift occurs on scales comparable to density variations (or at λ_J scale) has also been employed in previous studies (e.g., K. Silsbee et al. 2020; V. Vallucci-Goy et al. 2024).

2.3. Model and parameters

In this study, we introduced a molecular cloud model and a cloud core model defined by gas density n_{gas} and magnetic field strength $B = |\mathbf{B}|$. The molecular cloud model has $n_{\text{gas}} = 1.0 \times 10^4 \text{ cm}^{-3}$ (corresponding mass density, free-fall time and Jeans length is $\rho_{\text{gas}} = 3.91 \times 10^{-20} \text{ g cm}^{-3}$, $t_{\text{ff}} = 1.75 \times 10^5 \text{ yr}$ and $\lambda_J = 0.27 \text{ pc}$, respectively⁶) and $B = 20, 50 \mu\text{G}$, while the cloud core model has $n_{\text{gas}} = 1.0 \times 10^6 \text{ cm}^{-3}$ (corresponds to $\rho_{\text{gas}} = 3.91 \times 10^{-18} \text{ g cm}^{-3}$, $t_{\text{ff}} = 1.75 \times 10^4 \text{ yr}$ and $\lambda_J = 0.03 \text{ pc}$) and $B = 100, 200 \mu\text{G}$. We then compute dust growth and ionization chemistry in these environments (See Section 2.1 and 2.2.). The initial dust size distribution is set to the MRN distribution (J. S. Mathis et al. 1977), with a minimum size of $a_{\text{min}} = 5.0 \text{ nm}$ and a maximum size of $a_{\text{max}} = 250 \text{ nm}$. For the numerical implementation, the grid covers a size range from $a_{\text{grid,min}} = 3 \text{ nm}$ to $a_{\text{grid,max}} = 30 \mu\text{m}$, discretized into 256 bins.

In the simulation, we adopted four parameters: the cosmic-ray ionization rate ζ_{CR} , the dominant ion species s_{ion} , and the turbulent velocity (or Mach number \mathcal{M}) for the gas phase, and the material density ρ_{mat} for the dust phase.

⁶ We calculated free-fall time as

$$t_{\text{ff}} = \frac{1}{\sqrt{4\pi G \rho_{\text{gas}}}}. \quad (22)$$

Here, $\rho_{\text{gas}} = \mu m_p n_{\text{gas}}$ where $\mu = 2.3$ is the average molecular weight for typical gas consist of ISM and $m_p = 1.67 \times 10^{-24} \text{ g}$ is the mass of a proton. Jeans length is given by

$$\lambda_J = c_s \sqrt{\frac{\pi}{G \rho_{\text{gas}}}}, \quad (23)$$

with $c_s = (\gamma k_B T_{\text{gas}} / m_p \mu)^{1/2}$, where γ and T is the heat capacity ratio and gas temperature, respectively. k_B is the Boltzmann constant.

The cosmic-ray ionization rate of $\zeta_{\text{CR}} \sim 10^{-17} \text{ s}^{-1}$ has been widely adopted in studies of star-forming regions (so-called Spitzer value; L. Spitzer & M. G. Tomasko (1968)). Since molecular gas effectively shields cosmic rays, the ionization rate varies inversely with gas density. In the more diffuse Galactic ISM, values around $\sim 10^{-16} \text{ s}^{-1}$ have been reported (N. Indriolo & B. J. McCall 2012), whereas in dense molecular cloud cores, values ranging from $\sim 10^{-17} - 10^{-16} \text{ s}^{-1}$ have been observed (P. Caselli et al. 1998). Therefore, in this study, we adopt $\zeta_{\text{CR}} = 10^{-17}, 10^{-16} \text{ s}^{-1}$.

The gas velocity that determines the grain velocity is considered from subsonic to mildly supersonic ($\mathcal{M} = 0.5, 1.0, 2.0$). Recent observations in nearby filamentary molecular clouds indicate velocity structures around the transonic regime (D. Arzoumanian et al. 2013; A. Hacar & M. Tafalla 2011; A. Hacar et al. 2016). Cloud cores that form through fragmentation of these filaments are thought to inherit subsonic velocity structures. In fact, observations have revealed molecular cloud cores with transonic or subsonic turbulent velocities (M. Tafalla et al. 2004). Theoretical studies have also shown that cloud cores can form from filaments initially possessing turbulence with $\mathcal{M} = 2$ (Y. Misugi et al. 2024).

As the dominant gas-phase ion species, we consider HCO^+ and H_3^+ , both of which are expected to be major ion species in molecular clouds and cloud cores. Observations and theoretical studies (e.g., P. Caselli et al. (2002); K. Tassis et al. (2012b)) suggest that the H_3^+ becomes the dominant ion in high-density regions ($\sim 10^6 \text{ cm}^{-3}$), rather than HCO^+ . These ions behave differently in terms of their thermal velocity and recombination rate. The recombination rates for HCO^+ and H_3^+ are taken from the UMIST database (D. McElroy et al. 2013).⁷

For dust material, we focus on not only carbon- and silicate- based compounds but also icy grains, because the temperature of dark clouds embedding star-forming regions is sufficiently low for volatile molecules to stick to dust surface.

The definition of models and parameters are summarized in Table 1. We take the model with $\zeta_{\text{CR}} = 10^{-17}$, $s_{\text{ion}} = \text{H}_3^+$, $\rho_{\text{mat}} = 1.0$, $v_{\text{gas}} = 2c_s(\mathcal{M} = 2.0)$ as the fiducial model.

3. RESULTS

In this section, we present the simulation results for the evolution of the dust size distribution and its impact on the ion-neutral drift velocity v_{drift} .

⁷ <https://umistdatabase.uk>

Time evolution of the dust size distribution in the fiducial core model is shown in the left panel of Figure 2. Grains smaller than 10 nm are efficiently depleted by accretion by $t \simeq 1 t_{\text{ff}}$. Subsequently, coagulation accelerates grain growth and the maximum grain size reaches $\sim 10 \mu\text{m}$ by later times ($t \simeq 10 t_{\text{ff}}$). A shallow dip appears around $a \sim 30 \text{ nm}$ which is attributable to the adopted relative-velocity model for colliding grains (see Figure 1). This radius approximately marks the transition from the viscous (Brownian motion-dominated) to the inertial (turbulence-dominated) regime (see also Y. Kawasaki et al. (2022)). As grains enter the inertial regime their relative velocities increase, which accelerates coagulation.

The right panel of Figure 2 shows the time evolution of v_{drift} , estimated from our η_A calculation via Equation (21). The results show that the depletion of nano-sized very small grains contributing to electrical conductivity leads to an increase in the ambipolar resistivity, and consequently, a higher drift velocity. Simultaneously, coagulation reduces the total grain surface area, weakening the adsorption of charged particles onto grains. As a result, the gas-phase ionization degree increases and is solely determined by gas-phase recombination. Thus, both the magnetic resistivity and v_{drift} increase as dust grains grow and reach a plateau at later times (for this model, $t \gtrsim 10 t_{\text{ff}}$, i.e., $\sim 10^6 \text{ yr}$).

In this core model, the observed level of v_{drift} ($\sim 100 \text{ ms}^{-1}$) is reproduced with the magnetic field of $B \sim 200 \mu\text{G}$ once dust grains grow sufficiently. Several hundred micro-Gauss is a reasonable value for the magnetic field in the cores (R. M. Crutcher 2012).

On the other hand, if grains have not grown (i.e., at the initial time of the evolution), a strong magnetic field of 2000 μG is required to explain the value of the observed drift velocity. However, such a field strength —of several thousand micro-Gauss— is unacceptably large for the magnetic field in the cloud cores.

This result strongly suggests that dust growth is essential to produce the observed $v_{\text{drift}} \sim 100 \text{ ms}^{-1}$ in dense cores unless extraordinarily strong magnetic fields are required.

Figure 3 summarizes the dependence of v_{drift} on four parameters: (a) the cosmic-ray ionization rate ζ_{CR} , (b) the dominant ion species s_{ion} , (c) the grain intrinsic (material) density ρ_{mat} , and (d) the gas (turbulent) velocity v_{gas} . Line styles distinguish parameter values as indicated by the legend in each panel.

Cosmic-ray ionization rate.—In panel (a), variations in ζ_{CR} have little effect at early times ($t \lesssim 10^5 \text{ yr}$), when the adsorption of charged particles onto the grains regulates the ionization degree. By contrast, at later times

Table 1. Model and parameters

Model	n_{gas} [cm $^{-3}$]	B [μG]	ζ_{CR} [s $^{-1}$]	s_{ion}	ρ_{mat} [gcm $^{-3}$]	v_{gas}
Cloud	10^4	20				
		50	$1.0 \times 10^{-17*}$	HCO^+	1.0*	$\mathcal{M} = 0.5$
Core	10^6	100	1.0×10^{-16}	H_3^+*	2.0	$\mathcal{M} = 1.0$
		200			3.0	$\mathcal{M} = 2.0*$

NOTE—We assume two star-forming environment models defined by gas density and magnetic field strength, and perform one-zone calculation in each environment. For the cloud model ($n_{\text{gas}} = 10^4$ cm $^{-3}$), the free-fall time is $t_{\text{ff,cloud}} = 1.75 \times 10^5$ yr and Jeans length is $\lambda_{\text{J,cloud}} = 0.27$ pc. For the core model ($n_{\text{gas}} = 10^6$ cm $^{-3}$), the values are $t_{\text{ff,core}} = 1.75 \times 10^4$ yr and $\lambda_{\text{J,core}} = 0.027$ pc ~ 5600 AU, respectively. We assume the temperature to be $T_{\text{gas}} = 10$ K. Values marked with * are fiducial models.

($t \gtrsim 10^5$ yr), dust grains grow sufficiently and gas-phase recombination dominates the loss of charged particles. In this regime, a larger ζ_{CR} maintains a higher ionization degree, yielding a lower resistivity and therefore a smaller v_{drift} .

Ion species.—Panel (b) shows how the choice of dominant ion species affects v_{drift} . The dominant ion species in gas phase affects both the adsorption efficiency onto grains and gas-phase recombination rate. Lighter ions, such as H_3^+ , have larger thermal velocities, leading to more frequent collisions with dust grains and more efficient adsorption. This lowers the gas-phase ionization degree and consequently tends to increase v_{drift} at early times. On the other hand, in the later phase where dust growth has proceeded and gas-phase recombination dominates the ionization balance, the lower recombination rate of H_3^+ maintains a higher ionization degree more efficiently than HCO^+ . As a result, v_{drift} becomes smaller with H_3^+ at late times.

Grain material density.—Under a fixed dust-to-gas mass ratio, variations in the intrinsic grain material density ρ_{mat} change the normalization of the initial size distribution and hence the total grain surface area. With increasing ρ_{mat} , the overall number of grains decreases, resulting in a smaller total dust surface area. Consequently, the number of very small charged grains that contribute to the conductivity also decreases. This enhances the ambipolar resistivity and leads to a larger drift velocity (Figure 3(c)).

Gas velocity.—Increasing v_{gas} (i.e., the Mach number) raises grain-grain relative velocities and accelerates their coagulation, thereby shortening the timescale over which the v_{drift} evolve. We discuss these timescales in more detail in Section 4.

Taken together, the core-scale results indicate that reproducing the observed v_{drift} at core densities requires both substantial dust growth and a magnetic field strength of order $10^2 \mu\text{G}$ (specifically $B \simeq 200 \mu\text{G}$ in our

fiducial core model). This conclusion holds across the explored ranges of ζ_{CR} , dominant ion species s_{ion} , grain material density ρ_{mat} , and turbulent velocity v_{gas} .

This naturally prompts the question of whether, at the lower densities (i.e., molecular clouds), measurements of v_{drift} can likewise yield meaningful constraints on dust growth and on magnetic field strength. In the cloud density, however, we conclude that dust growth is not always required.

The left panel of Figure 4 shows the evolution of the grain-size distribution in the cloud model (its number density is $n_{\text{gas}} = 10^4$ cm $^{-3}$). As in the core model, accretion rapidly depletes the small grains ($a \lesssim 10$ nm) at early phase, after which coagulation produces grains up to $\sim 1 \mu\text{m}$. A key difference from the core model is that the maximum grain size remains $\sim 1 \mu\text{m}$ even by $t \simeq 10 t_{\text{ff}}$.

Right panel shows the time evolution of the drift velocity. No single set of conditions uniquely reproduces the observed v_{drift} in this model: for $B = 20 \mu\text{G}$ the observed range is reached only after dust growth proceeds, whereas for $B = 50 \mu\text{G}$ it is already achieved in the early phase without significant dust growth. Both values of magnetic field strength are acceptable for the values of molecular clouds (R. M. Crutcher 2012). Figure 5 illustrates the evolution of v_{drift} in the cloud model and its dependence on the four parameters, shown in panels ((a) ζ_{CR} , (b) s_{ion} , (c) ρ_{mat} , and (d) v_{gas}). For each parameter, the qualitative trends are similar to those found in the core model (Figure 3). Consequently, at cloud densities, v_{drift} alone does not tightly constrain the magnetic field strength because of degeneracies with dust evolution.

4. DISCUSSION

We have estimated ion-neutral drift velocity in molecular clouds and dense cores by coupling dust size evolution driven by accretion and coagulation with an ionization chemistry that self-consistently accounts for dust charging (e.g., B. T. Draine & B. Sutin 1987;

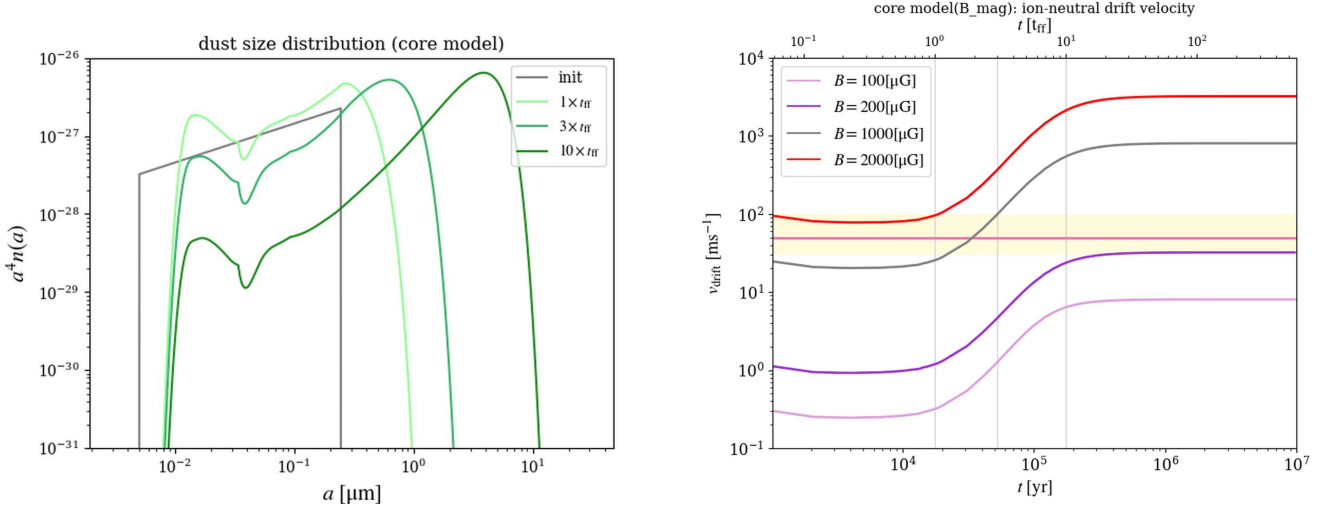


Figure 2. (Left) The dust size distribution at the epoch of $1 \times t_{\text{ff}}$ (light green), $3 \times t_{\text{ff}}$ (middle green), $10 \times t_{\text{ff}}$ (deep green). The initial size distribution is shown in gray. (Right) Dependence of the time evolution of ion-neutral drift velocity in core model on magnetic field strength. In addition to the case of $B = 100 \mu\text{G}$ (light purple) and $B = 200 \mu\text{G}$ (purple), we plot the case of $B = 1000 \mu\text{G}$ (gray) and $B = 2000 \mu\text{G}$ (red) for reference. The lower and upper horizontal axis show the evolution time in unit of yr and t_{ff} , respectively. The observed v_{drift} is indicated by yellow-filled region. The pink line shows $v_{\text{drift}} = 50 \text{ ms}^{-1}$. Three thin gray vertical lines correspond to $t = 1, 3$ and $10 \times t_{\text{ff}}$.

[Y. Tsukamoto & S. Okuzumi 2022](#)). We then examine how the observed ion-neutral drift velocity, $v_{\text{drift}} \sim 100 \text{ m s}^{-1}$, constrains the dust size distribution, the cosmic-ray ionization rate, and the magnetic field strength. Our results indicate that dust growth plays a key role in reproducing the observed drift velocity, especially in cloud cores.

At core densities ($n_{\text{gas}} \sim 10^6 \text{ cm}^{-3}$), our models obtain $v_{\text{drift}} \sim 100 \text{ m s}^{-1}$ only when (i) the grains have undergone substantial growth, leading to a strong reduction in total surface area (with the mass-weighted sizes extending to $\sim 10 \mu\text{m}$); (ii) the magnetic field strength is on the order of $B \sim 200 \mu\text{G}$; and (iii) cosmic-ray ionization rate is $\zeta_{\text{CR}} \sim 10^{-17} \text{ s}^{-1}$.

In the absence of grain growth (i.e., an MRN-like abundance of small grains), $v_{\text{drift}} \sim 100 \text{ m s}^{-1}$ would instead require $B \gtrsim 1 \text{ mG}$, significantly larger than typical estimates for dense cores ([R. M. Crutcher 2012](#)). These trends follow directly from the sensitivity of the ambipolar diffusivity to the abundance of small grains, which contribute to the electrical conductivity as charge carriers ([B. Zhao et al. 2021](#); [Y. Tsukamoto & S. Okuzumi 2022](#)).

At cloud densities ($n_{\text{gas}} \sim 10^4 \text{ cm}^{-3}$), the observed range of v_{drift} can be attained either with modest magnetic field strength once grain growth proceeds or with slightly stronger fields in the absence of grain growth. Therefore, v_{drift} alone does not provide strong constraint on magnetic field strength at cloud scales, because of its degeneracies with the dust size and magnetic field strength (Figure 4, 5).

Given that our core models place relatively tight constraints on the combination of magnetic field strength, cosmic-ray ionization rate, and dust growth required to reach $v_{\text{drift}} \sim 100 \text{ m s}^{-1}$, it is instructive to compare these conditions with those inferred for the well-studied starless (prestellar) core L1544 in Taurus. [M. Tafalla et al. \(2002\)](#) estimated a central H_2 number density of $n_{\text{H}_2} \simeq 1.4 \times 10^6 \text{ cm}^{-3}$, with a characteristic flat inner radius of $r \simeq 2.9 \times 10^3 \text{ AU}$. Submillimeter polarization observations analyzed with the Chandrasekhar-Fermi method yield a plane-of-sky magnetic field strength of order $B_{\text{pos}} \sim 100\text{--}400 \mu\text{G}$ on similar scales ([R. M. Crutcher et al. 2004](#)). The cosmic-ray ionization rate in L1544 has been estimated to be $\zeta_{\text{CR}} \simeq (2\text{--}3) \times 10^{-17} \text{ s}^{-1}$ ([S. Bovino et al. 2020](#); [E. Redaelli et al. 2021](#)). These values are broadly comparable to the parameter space explored in our core models (see Table 1). Therefore, if the ion-neutral drift is observed in L1544 for example, particularly at the level discussed above, it lends support to the relevance of dust-growth-induced ambipolar diffusion for real prestellar cores.

In addition to the agreement in these profiles, it is worth noting that the L1544 core is known to exhibit the "coreshine" phenomenon ([L. Pagani et al. 2010](#)) which is interpreted as evidence for the presence of micron-sized dust grains. This observational indication of dust growth provides independent support for the grain growth predicted in our model.

We next consider the ionization fraction. For the L1544 core, the ionization fraction has been estimated to be $x_i \equiv n_i/n_{\text{H}_2} \simeq 1.1 \times 10^{-8}$ ([P. Caselli et al. 2002](#)). Are

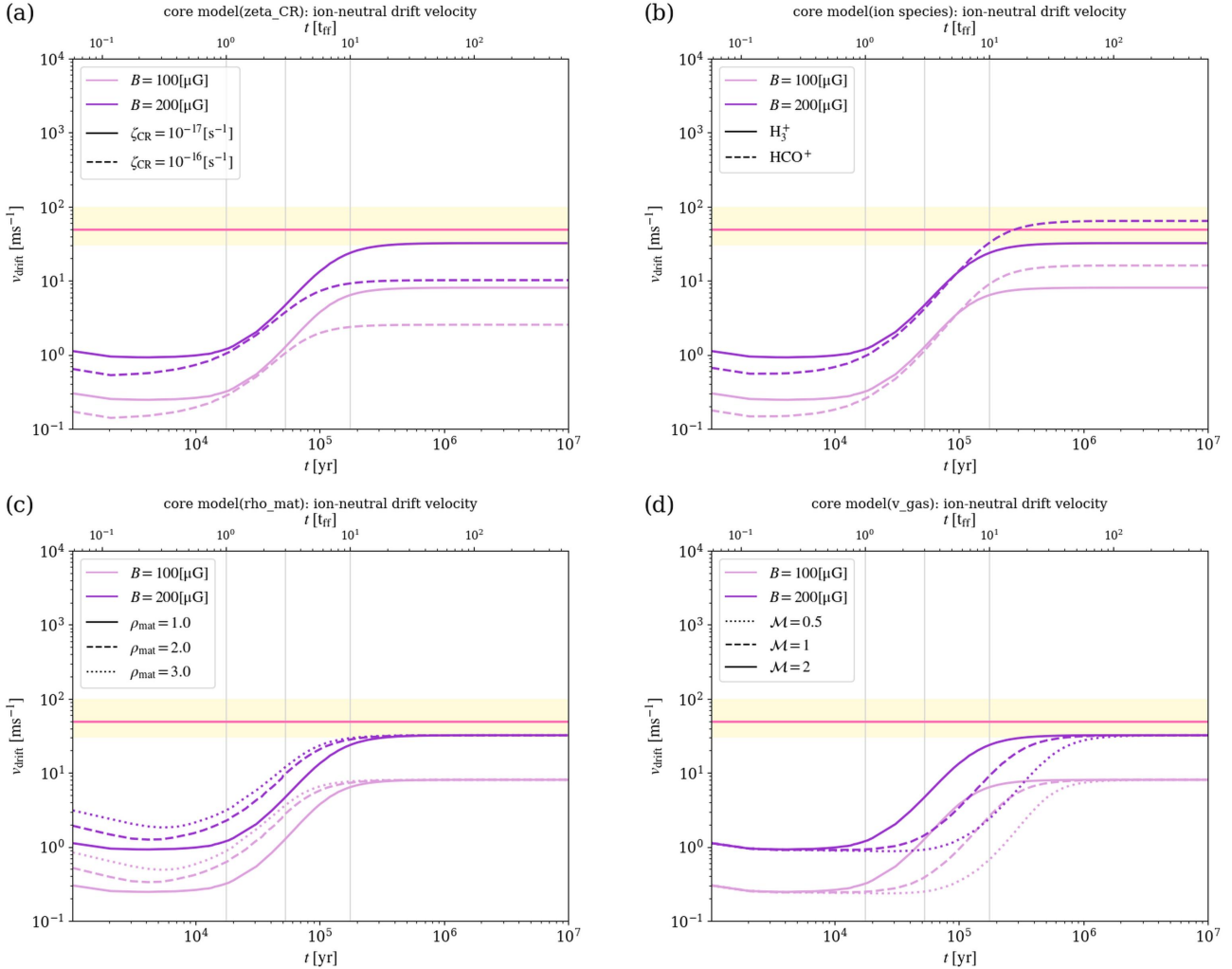


Figure 3. Dependency of estimated v_{drift} on (a)the cosmic ray ionization rate; ζ_{CR} (b)the dominant ion species; s_{ion} in gas phase (c)the intrinsic grain material density; ρ_{mat} (d)the gas velocity; v_{gas} , in cloud core model. The difference in each parameter is indicated by the line styles.

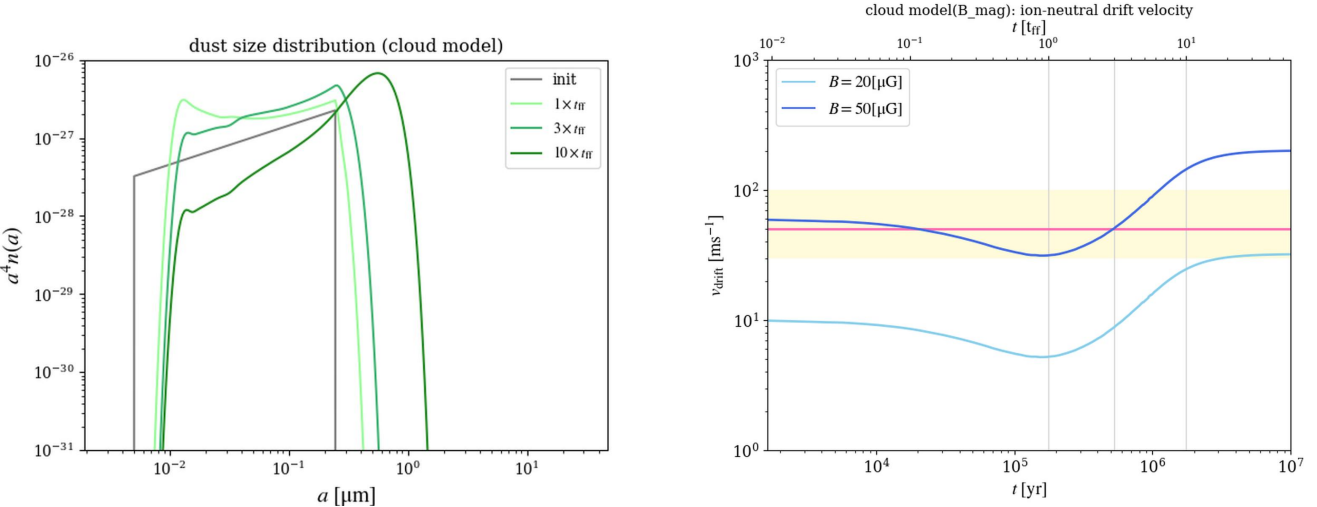


Figure 4. Time evolution of dust size distribution(left) and ion-neutral drift velocity(right) for cloud model, shown in the same format as Figure 2. The light-blue and blue lines represent magnetic field strengths of $20 \mu\text{G}$ and $50 \mu\text{G}$, respectively.

our results consistent with this value, and under what

conditions can such consistency be achieved? Figure 6

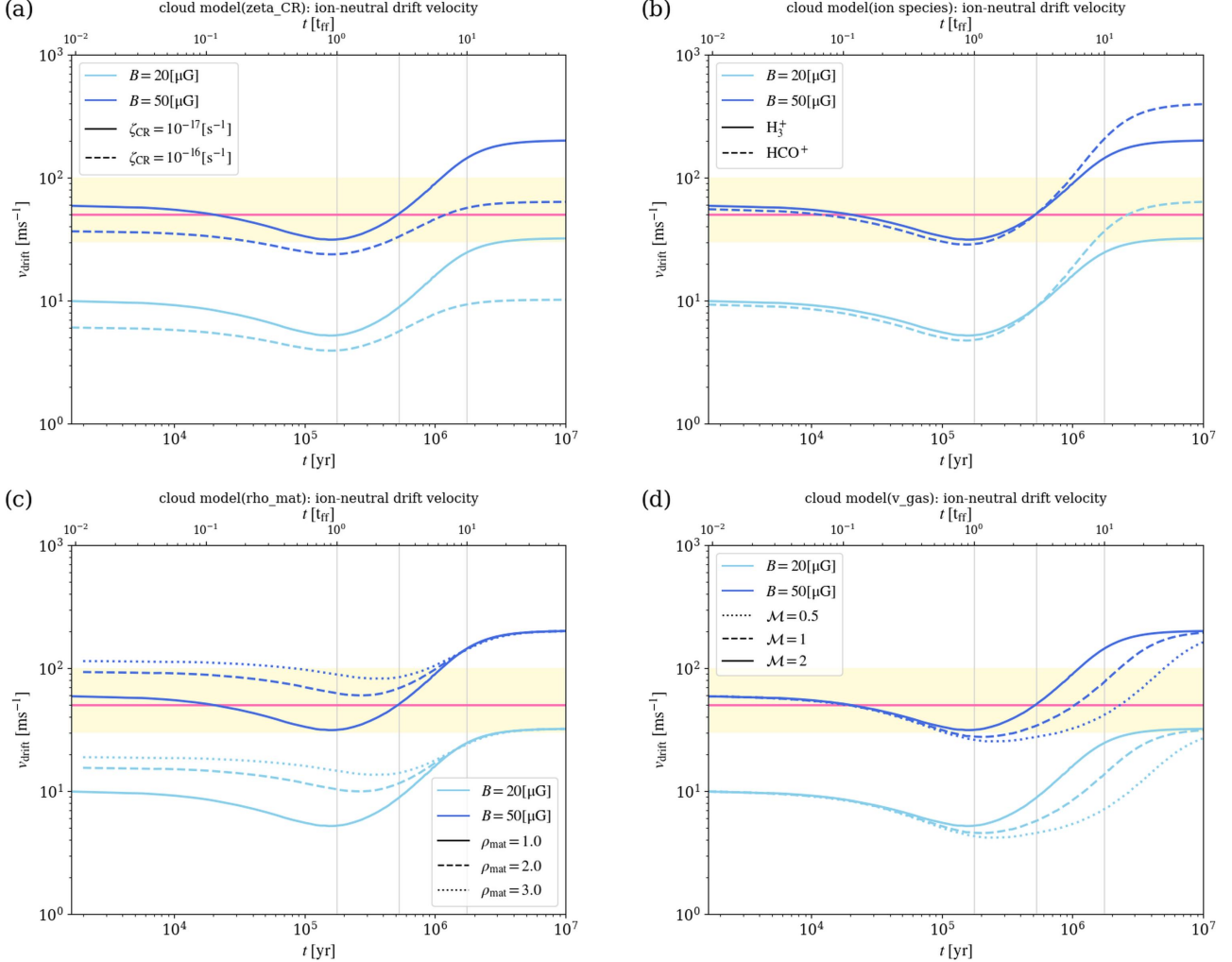


Figure 5. The dependence of the time evolution of v_{drift} in the cloud model on (a) ζ_{CR} (b) s_{ion} (c) ρ_{mat} (d) v_{gas} , as in Figure 3. shows the ionization fraction from our simulations. The ionization fraction x_i is calculated as

$$x_i = \frac{n_i}{n_{\text{H}_2}}, \quad (24)$$

where $n_{\text{H}_2} = (\mu/\mu_{\text{H}_2}) n_{\text{gas}}$. Here, $\mu = 2.3$ and $\mu_{\text{H}_2} = 2.8$ are the mean molecular weights of the neutral gas and hydrogen gas, respectively. In the cloud model, x_i is in the range 10^{-8} – 10^{-7} , whereas in the core model it is in the range $\sim 10^{-10}$ – 10^{-8} . In both models, the ionization fraction increases as the dust grows. These values are consistent with classical theoretical predictions (e.g., R. Nishi et al. 1991). More specifically, the values obtained with the ion species $s_{\text{ion}} = \text{H}_3^+$ and cosmic-ray ionization rate $\zeta_{\text{CR}} = 1.0 \times 10^{-16} \text{ s}^{-1}$ after sufficient dust growth are in good agreement with the ionization fraction in the L1544 core reported by P. Caselli et al. (2002). This suggests that dust growth may play a key role in producing the low ionization fraction observed in the L1544 core.

Our cloud and core models employ a one-zone treatment that we regard as a useful benchmark rather than a precise description of real clouds or cores; it neglects spatial structure, line-of-sight averaging, and the full dynamical evolution from cloud to core. We acknowledge that a number of studies have emphasized that extracting a reliable ion–neutral drift from line profiles is intrinsically challenging. In order for v_{drift} to be robustly inferred, the ion and neutral tracers must sample the same gas volume and be chemically co-evolving; otherwise, differences in critical densities or abundances can mimic or mask true drift (e.g., H.-b. Li & M. Houde 2008; K. Tassis et al. 2012a). Line radiative transfer and projection further complicate the interpretation: line-of-sight integration, magnetic-field geometry, and turbulent fluctuations can reduce the observable signature of a given 3D drift, so that even a true subsonic drift may appear at a reduced level in the observed linewidths (e.g., D. A. Tilley & D. S. Balsara 2010; T. Hezareh et al.

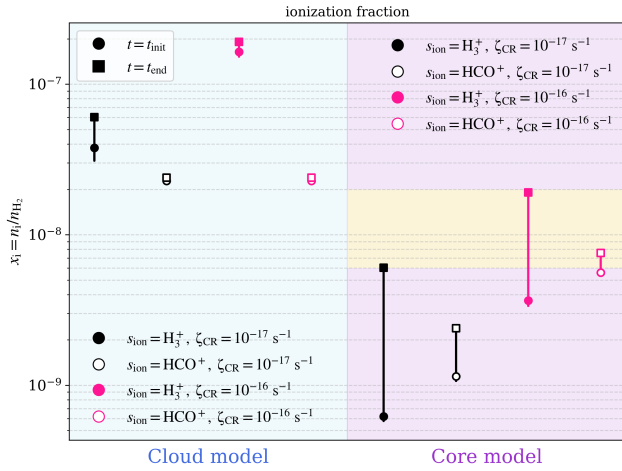


Figure 6. Ionization fraction n_i/n_{H_2} in the molecular cloud model ($n_{\text{gas}} = 10^4 \text{ cm}^{-3}$; blue-shaded region on the left) and the molecular cloud core model ($n_{\text{gas}} = 10^6 \text{ cm}^{-3}$; purple-shaded region on the right). Circles and squares indicate the values at $t = t_{\text{init}}$ and $t = t_{\text{end}}$, respectively. Filled symbols correspond to $s_{\text{ion}} = \text{H}_3^+$, while open symbols correspond to $s_{\text{ion}} = \text{HCO}^+$. Black and pink symbols represent $\zeta_{\text{CR}} = 10^{-17} \text{ s}^{-1}$ and $\zeta_{\text{CR}} = 10^{-16} \text{ s}^{-1}$, respectively. The yellow shaded region indicates a factor-of-two range around the observed value 1.1×10^{-8} reported for the L1544 core (P. Caselli et al. 2002).

2014). More recently, A. Tritsis et al. (2023) combined chemodynamical non-ideal MHD simulations and non-LTE radiative transfer for the simulation results, and showed that secure detection of ion–neutral drift generally requires stringent observing conditions and careful tracer selection. These works underscore that currently reported values of v_{drift} carry systematic uncertainties of a factor of a few that must be borne in mind when comparing with models.

Within our idealized one-zone framework, however, we find that dust growth alone can change the predicted v_{drift} by nearly an order of magnitude at fixed density n_{gas} , magnetic field strength B , and cosmic-ray ionization rate ζ_{CR} . Thus, even if the absolute observationally inferred drift velocities are revised downward by geometry or radiative-transfer effects, the qualitative conclusion that the dust size distribution has a strong impact on v_{drift} remains robust.

Our one-zone treatment with fixed n_{gas} and B also has a limitation in evaluating the dust growth timescale. In reality, dust coagulation proceeds within a time-dependent cloud-to-core evolution, which involves the dynamics of gas density (free-fall time) and magnetic field. As we have seen, the coagulation timescale to reach micron sizes at $n_{\text{gas}} \sim 10^4\text{--}10^6 \text{ cm}^{-3}$ exceeds a free-fall time, whereas recent simulations suggest that

filament-to-core formation proceeds over several free-fall times ($\sim 10 \mu\text{G}$ at $n_{\text{gas}} = 10^4 \text{ cm}^{-3}$) (Y. Misugi et al. 2024; H. Fukihara et al. 2025).

These challenges motivate fully coupled 3D non-ideal MHD calculations that evolve gas density, magnetic fields, chemistry, and dust grain simultaneously to identify when and where efficient grain growth occurs during cloud contraction. Furthermore, combining time-dependent multi-dimensional non-ideal MHD and forward modelling of line emission will enable the dust microphysics and observational systems to be treated as complementary components on equal footing in forming the measured ion–neutral drift.

In addition, our treatment of dust size evolution can be extended in several ways. Our coagulation model employs a relative-velocity prescription that includes only Brownian and turbulence-driven components. However, several additional processes can modify the dust size evolution. For example, we neglect detailed collision physics such as electrostatic repulsion: Coulomb barriers between like-charged grains can inhibit sticking at small sizes (e.g., S. Okuzumi 2009). In magnetized clouds, the small charged grains can become magnetically tied to field lines and participate in ambipolar drift together with ions (e.g., G. E. Ciolek & T. C. Mouschovias 1996; V. Guillet et al. 2020; K. Silsbee et al. 2020). Quantifying the combined impact of these effects within a framework that self-consistently incorporates dust charging and ambipolar diffusion will require more comprehensive dust-kinetics models and constitutes an important direction for future work.

Although these future challenges remain, we think that the observation of ion–neutral drift velocity is a promising diagnostic for constraining the dust size distribution and magnetic field strength in molecular cloud cores.

ACKNOWLEDGMENTS

This study was supported by the JST FOREST Program, Grant Number JPMJFR2234. We sincerely thank all those whose valuable discussions, whether in our daily work or at conferences and workshops, have contributed to the development of this study. In particular, we are grateful to Dr. Shinsuke Takasao, who kindly joined our discussions and made them more rewarding. We further wish to express our thanks to Dr. Silvia Spezzano, who participated in our discussions and warmly contributed to a pleasant and fruitful exchange. Finally we thank the anonymous referee for constructive comments and suggestions that greatly improved the manuscript.

REFERENCES

Arzoumanian, D., André, P., Peretto, N., & Könyves, V. 2013, *A&A*, 553, A119, DODOI10.1051/0004-6361/201220822

Arzoumanian, D., Furuya, R. S., Hasegawa, T., et al. 2021, *A&A*, 647, A78, DODOI10.1051/0004-6361/202038624

Bovino, S., Ferrada-Chamorro, S., Lupi, A., Schleicher, D. R. G., & Caselli, P. 2020, *MNRAS*, 495, L7, DODOI10.1093/mnrasl/slaa048

Cacciapuoti, L., Testi, L., Podio, L., et al. 2024, *ApJ*, 961, 90, DODOI10.3847/1538-4357/ad0f17

Caselli, P., Walmsley, C. M., Terzieva, R., & Herbst, E. 1998, *ApJ*, 499, 234, DODOI10.1086/305624

Caselli, P., Walmsley, C. M., Zucconi, A., et al. 2002, *ApJ*, 565, 344, DODOI10.1086/324302

Ceccarelli, C., Viti, S., Balucani, N., & Taquet, V. 2018, *MNRAS*, 476, 1371, DODOI10.1093/mnras/sty313

Chandrasekhar, S., & Fermi, E. 1953, *ApJ*, 118, 113, DODOI10.1086/145731

Chen, C.-Y., Li, Z.-Y., Mazzei, R. R., et al. 2022, *MNRAS*, 514, 1575, DODOI10.1093/mnras/stac1417

Ching, T.-C., Qiu, K., Li, D., et al. 2022, *ApJ*, 941, 122, DODOI10.3847/1538-4357/ac9dfb

Ciolek, G. E., & Mouschovias, T. C. 1993, *ApJ*, 418, 774, DODOI10.1086/173435

Ciolek, G. E., & Mouschovias, T. C. 1994, *ApJ*, 425, 142, DODOI10.1086/173971

Ciolek, G. E., & Mouschovias, T. C. 1995, *ApJ*, 454, 194, DODOI10.1086/176477

Ciolek, G. E., & Mouschovias, T. C. 1996, *ApJ*, 468, 749, DODOI10.1086/177730

Coudé, S., Bastien, P., Houde, M., et al. 2019, *ApJ*, 877, 88, DODOI10.3847/1538-4357/ab1b23

Crutcher, R. M. 2012, *ARA&A*, 50, 29, DODOI10.1146/annurev-astro-081811-125514

Crutcher, R. M., Nutter, D. J., Ward-Thompson, D., & Kirk, J. M. 2004, *ApJ*, 600, 279, DODOI10.1086/379705

Doi, Y., Hasegawa, T., Furuya, R. S., et al. 2020, *ApJ*, 899, 28, DODOI10.3847/1538-4357/aba1e2

Draine, B. T., & Sutin, B. 1987, *ApJ*, 320, 803, DODOI10.1086/165596

Elmegreen, B. G. 1979, *ApJ*, 232, 729, DODOI10.1086/157333

Falgarone, E., Troland, T. H., Crutcher, R. M., & Paubert, G. 2008, *A&A*, 487, 247, DODOI10.1051/0004-6361:200809577

Fukihara, H., Takaishi, D., Misugi, Y., Sasaki, M., & Tsukamoto, Y. 2025, *PASJ*, 77, 277, DODOI10.1093/pasj/psae115

Guillet, V., Hennebelle, P., Pineau des Forêts, G., et al. 2020, *A&A*, 643, A17, DODOI10.1051/0004-6361/201937387

Hacar, A., Kainulainen, J., Tafalla, M., Beuther, H., & Alves, J. 2016, *A&A*, 587, A97, DODOI10.1051/0004-6361/201526015

Hacar, A., & Tafalla, M. 2011, *A&A*, 533, A34, DODOI10.1051/0004-6361/201117039

Heiles, C., & Troland, T. H. 2005, *ApJ*, 624, 773, DODOI10.1086/428896

Hezareh, T., Csengeri, T., Houde, M., Herpin, F., & Bontemps, S. 2014, *MNRAS*, 438, 663, DODOI10.1093/mnras/stt2237

Hirashita, H. 2012, *MNRAS*, 422, 1263, DODOI10.1111/j.1365-2966.2012.20702.x

Hirashita, H., & Aoyama, S. 2019, *MNRAS*, 482, 2555, DODOI10.1093/mnras/sty2838

Houde, M., Vaillancourt, J. E., Hildebrand, R. H., Chitsazzadeh, S., & Kirby, L. 2009, *ApJ*, 706, 1504, DODOI10.1088/0004-637X/706/2/1504

Hwang, J., Kim, J., Pattle, K., et al. 2021, *ApJ*, 913, 85, DODOI10.3847/1538-4357/abf3c4

Indriolo, N., & McCall, B. J. 2012, *ApJ*, 745, 91, DODOI10.1088/0004-637X/745/1/91

Kawasaki, Y., Koga, S., & Machida, M. N. 2022, *MNRAS*, 515, 2072, DODOI10.1093/mnras/stac1919

Kobayashi, Y., Takaishi, D., & Tsukamoto, Y. 2023, *MNRAS*, 521, 2661, DODOI10.1093/mnras/stad711

Kwon, W., Looney, L. W., Mundy, L. G., Chiang, H.-F., & Kemball, A. J. 2009, *ApJ*, 696, 841, DODOI10.1088/0004-637X/696/1/841

Kwon, W., Looney, L. W., Mundy, L. G., & Welch, W. J. 2015, *ApJ*, 808, 102, DODOI10.1088/0004-637X/808/1/102

Li, H.-b., & Houde, M. 2008, *ApJ*, 677, 1151, DODOI10.1086/529581

Li, Z.-Y., Krasnopolsky, R., & Shang, H. 2011, *ApJ*, 738, 180, DODOI10.1088/0004-637X/738/2/180

Lyo, A. R., Kim, J., Sadavoy, S., et al. 2021, *ApJ*, 918, 85, DODOI10.3847/1538-4357/ac0ce9

Masson, J., Chabrier, G., Hennebelle, P., Vaytet, N., & Commerçon, B. 2016, *A&A*, 587, A32, DODOI10.1051/0004-6361/201526371

Mathis, J. S., Rumpl, W., & Nordsieck, K. H. 1977, *ApJ*, 217, 425, DODOI10.1086/155591

McElroy, D., Walsh, C., Markwick, A. J., et al. 2013, *A&A*, 550, A36, DODOI10.1051/0004-6361/201220465

Mestel, L., & Spitzer, Jr., L. 1956, *MNRAS*, 116, 503, DODOI10.1093/mnras/116.5.503

Misugi, Y., Inutsuka, S.-i., Arzoumanian, D., & Tsukamoto, Y. 2024, *ApJ*, 963, 106, DODOI10.3847/1538-4357/ad1990

Nakano, T., Nishi, R., & Umebayashi, T. 2002, *ApJ*, 573, 199, DODOI10.1086/340587

Nakano, T., & Umebayashi, T. 1986, *MNRAS*, 218, 663, DODOI10.1093/mnras/218.4.663

Nishi, R., Nakano, T., & Umebayashi, T. 1991, *ApJ*, 368, 181, DODOI10.1086/169682

Okuzumi, S. 2009, *ApJ*, 698, 1122, DODOI10.1088/0004-637X/698/2/1122

Ormel, C. W., & Cuzzi, J. N. 2007, *A&A*, 466, 413, DODOI10.1051/0004-6361:20066899

Pagani, L., Steinacker, J., Bacmann, A., Stutz, A., & Henning, T. 2010, *Science*, 329, 1622, DODOI10.1126/science.1193211

Pattle, K., Lai, S.-P., Hasegawa, T., et al. 2019, *ApJ*, 880, 27, DODOI10.3847/1538-4357/ab286f

Pattle, K., Lai, S.-P., Di Francesco, J., et al. 2021, *ApJ*, 907, 88, DODOI10.3847/1538-4357/abcc6c

Pineda, J. E., Schmiedeke, A., Caselli, P., et al. 2021, *ApJ*, 912, 7, DODOI10.3847/1538-4357/abebdd

Pinto, C., & Galli, D. 2008, *A&A*, 484, 17, DODOI10.1051/0004-6361:20078819

Redaelli, E., Sipilä, O., Padovani, M., et al. 2021, *A&A*, 656, A109, DODOI10.1051/0004-6361/202141776

Shu, F. H., Adams, F. C., & Lizano, S. 1987, *ARA&A*, 25, 23, DODOI10.1146/annurev.aa.25.090187.000323

Silsbee, K., Ivlev, A. V., Sipilä, O., Caselli, P., & Zhao, B. 2020, *A&A*, 641, A39, DODOI10.1051/0004-6361/202038063

Skalidis, R., & Tassis, K. 2021, *A&A*, 647, A186, DODOI10.1051/0004-6361/202039779

Spitzer, Jr., L., & Tomasko, M. G. 1968, *ApJ*, 152, 971, DODOI10.1086/149610

Steinacker, J., Pagani, L., Bacmann, A., & Guieu, S. 2010, *A&A*, 511, A9, DODOI10.1051/0004-6361/200912835

Steinacker, J., Andersen, M., Thi, W. F., et al. 2015, *A&A*, 582, A70, DODOI10.1051/0004-6361/201425434

Tafalla, M., Myers, P. C., Caselli, P., & Walmsley, C. M. 2004, *A&A*, 416, 191, DODOI10.1051/0004-6361:20031704

Tafalla, M., Myers, P. C., Caselli, P., Walmsley, C. M., & Comito, C. 2002, *ApJ*, 569, 815, DODOI10.1086/339321

Tassis, K., Hezareh, T., & Willacy, K. 2012a, *ApJ*, 760, 57, DODOI10.1088/0004-637X/760/1/57

Tassis, K., Willacy, K., Yorke, H. W., & Turner, N. J. 2012b, *ApJ*, 753, 29, DODOI10.1088/0004-637X/753/1/29

Tilley, D. A., & Balsara, D. S. 2010, *MNRAS*, 406, 1201, DODOI10.1111/j.1365-2966.2010.16768.x

Tomida, K., Okuzumi, S., & Machida, M. N. 2015, *ApJ*, 801, 117, DODOI10.1088/0004-637X/801/2/117

Tritsis, A., Basu, S., & Federrath, C. 2023, *MNRAS*, 521, 5087, DODOI10.1093/mnras/stad829

Tritsis, A., Basu, S., & Federrath, C. 2025, *A&A*, 695, A18, DODOI10.1051/0004-6361/202452013

Tritsis, A., Federrath, C., Willacy, K., & Tassis, K. 2022, *MNRAS*, 510, 4420, DODOI10.1093/mnras/stab3740

Troland, T. H., & Crutcher, R. M. 2008, *ApJ*, 680, 457, DODOI10.1086/587546

Tsukamoto, Y. 2024, *PASJ*, 76, 674, DODOI10.1093/pasj/psae039

Tsukamoto, Y., Iwasaki, K., Okuzumi, S., Machida, M. N., & Inutsuka, S. 2015, *MNRAS*, 452, 278, DODOI10.1093/mnras/stv1290

Tsukamoto, Y., Machida, M. N., & Inutsuka, S.-i. 2023, *PASJ*, 75, 835, DODOI10.1093/pasj/psad040

Tsukamoto, Y., & Okuzumi, S. 2022, *ApJ*, 934, 88, DODOI10.3847/1538-4357/ac7b7b

Umebayashi, T., & Nakano, T. 1980, *PASJ*, 32, 405, DODOI10.1093/pasj/32.3.405

Umebayashi, T., & Nakano, T. 1990, *MNRAS*, 243, 103, DODOI10.1093/mnras/243.1.103

Vallucci-Goy, V., Lebreuilly, U., & Hennebelle, P. 2024, *A&A*, 690, A23, DODOI10.1051/0004-6361/202348268

Wang, J.-W., Koch, P. M., Clarke, S. D., et al. 2024, *ApJ*, 962, 136, DODOI10.3847/1538-4357/ad165b

Ward-Thompson, D., Karoly, J., Pattle, K., et al. 2023, *ApJ*, 946, 62, DODOI10.3847/1538-4357/acbea4

Wurster, J., Price, D. J., & Bate, M. R. 2016, *MNRAS*, 457, 1037, DODOI10.1093/mnras/stw013

Xu, W., & Kunz, M. W. 2021, *MNRAS*, 508, 2142, DODOI10.1093/mnras/stab2715

Yen, H.-W., Zhao, B., Koch, P. M., et al. 2018, *A&A*, 615, A58, DODOI10.1051/0004-6361/201732195

Zhao, B., Caselli, P., Li, Z.-Y., et al. 2021, *MNRAS*, 505, 5142, DODOI10.1093/mnras/stab1295

Zhao, B., Caselli, P., Li, Z.-Y., et al. 2016, *MNRAS*, 460, 2050, DODOI10.1093/mnras/stw1124